

Article

# Temperature Effects on Tensile Deformation Behavior of a Medium Manganese TRIP Steel and a Quenched and Partitioned Steel

Whitney A. Poling <sup>1,\*</sup>, Emmanuel De Moor <sup>2</sup>, John G. Speer <sup>2</sup> and Kip O. Findley <sup>2</sup><sup>1</sup> General Motors Global R&D, 30470 Harley Earl Blvd, Warren, MI 48092, USA<sup>2</sup> Advanced Steel Processing and Products Research Center, Colorado School of Mines, 1500 Illinois Street, Golden, CO 80401, USA; edemoor@mines.edu (E.D.M.); jspeer@mines.edu (J.G.S.); kfindley@mines.edu (K.O.F.)

\* Correspondence: whitney.poling@gm.com; Tel.: +1-586-246-1486

**Abstract:** Third-generation advanced high-strength steels (AHSS) containing metastable retained austenite are being developed for the structural components of vehicles to reduce vehicle weight and improve crash performance. The goal of this work was to compare the effect of temperature on austenite stability and tensile mechanical properties of two steels, a quenched and partitioned (Q&P) steel with a martensite and retained austenite microstructure, and a medium manganese transformation-induced plasticity (TRIP) steel with a ferrite and retained austenite microstructure. Quasi-static tensile tests were performed at temperatures between  $-10$  and  $85$  °C for the Q&P steel (0.28C-2.56Mn-1.56Si in wt.%), and between  $-10$  and  $115$  °C for the medium manganese TRIP steel (0.14C-7.14Mn-0.23Si in wt.%). X-ray diffraction measurements as a function of strain were performed from interrupted tensile tests at all test temperatures. For the medium manganese TRIP steel, austenite stability increased significantly, serrated flow behavior changed, and tensile strength and elongation changed significantly with increasing temperature. For the Q&P steel, flow stress was mostly insensitive to temperature, uniform elongation decreased with increasing temperature, and austenite stability increased with increasing temperature. The Olson–Cohen model for the austenite-to-martensite transformation as a function of strain showed good agreement for the medium manganese TRIP steel data and fit most of the Q&P steel data above 1% strain.

**Keywords:** medium manganese TRIP steel; quenched and partitioned (Q&P) steel; tensile mechanical behavior; strain-induced austenite-to-martensite transformation



**Citation:** Poling, W.A.; De Moor, E.; Speer, J.G.; Findley, K.O. Temperature Effects on Tensile Deformation Behavior of a Medium Manganese TRIP Steel and a Quenched and Partitioned Steel. *Metals* **2021**, *11*, 375. <https://doi.org/10.3390/met11020375>

Academic Editor: Heung Nam Han

Received: 17 January 2021

Accepted: 17 February 2021

Published: 23 February 2021

**Publisher's Note:** MDPI stays neutral with regard to jurisdictional claims in published maps and institutional affiliations.



**Copyright:** © 2021 by the authors. Licensee MDPI, Basel, Switzerland. This article is an open access article distributed under the terms and conditions of the Creative Commons Attribution (CC BY) license (<https://creativecommons.org/licenses/by/4.0/>).

## 1. Introduction

Advanced high-strength steels (AHSS) are being incorporated into vehicles for weight reduction and improved crash performance [1–3]. With some of the more recently introduced third-generation AHSS, there are new issues encountered in automotive manufacturing and service, e.g., the wide variation in tensile behavior with respect to temperature and negative strain-rate sensitivity of medium manganese transformation-induced plasticity (TRIP) steel [4]. The goal of this study is to gain a better understanding of temperature effects on tensile behavior and austenite stability of two types of third-generation AHSS. The enhanced combination of strength and ductility of third-generation AHSS comes from multiconstituent microstructures, and retained austenite is a key microstructural constituent that undergoes a strain-induced transformation to martensite [5]. Under forming operations and crash conditions, steel components are subjected to deformation at a wide range of strain rates ( $0.01$ – $1000$  s<sup>-1</sup>), and adiabatic heating can occur at higher rates [6,7]. For example, temperature increases up to  $82$  °C at the ultimate tensile strength (UTS) were observed during high-rate tensile testing of the 1.4 mm thick medium Mn steel in this study [8]. Adiabatic heating during high strain rate deformation may increase austenite

stability and thus impact mechanical behavior [9–11]. The effect of temperature on flow stress in the range of  $-40$  to  $100$  °C is also an important performance metric for sheet steels considered for use in vehicles [4].

Studies on single-phase metastable austenitic stainless steels have shown that the strain-induced austenite-to-martensite transformation rate decreases as test temperature increases [12,13], and this increasing austenite stability is associated with a decrease in elongation along with changes in work hardening rates that contribute to lower flow stresses and the flattening of the sigmoidal-shaped stress–strain curve [14–17]. Similar observations were made for an 8 wt.% Ni steel alloy [18] and a duplex stainless steel [19] that both contained over 50 vol.% metastable austenite. Low-alloy multiphase TRIP steels containing lower austenite fractions (<20 vol.%) in addition to ferrite, bainite, and/or martensite also exhibit an increase in austenite stability with increasing temperature [20,21], but the effect of higher austenite stability on the tensile mechanical behavior is more subtle due to the lower initial austenite content (e.g., smaller decreases in elongation and work hardening were observed) [22–24]. For both metastable austenitic stainless steels and multiphase TRIP steels, the austenite-to-martensite transformation can be fit by the Olson–Cohen relationship describing austenite transformation kinetics with strain [14,17,21,25]. However, there are significant differences in the microstructures, compositions, and deformation behavior of third-generation AHSS that require further characterization. In this study, a quenched and partitioned (Q&P) steel and a medium manganese TRIP steel were investigated. The microstructure of the Q&P steel consisted of a martensitic matrix with blocky and thin film retained austenite, while the microstructure of the medium manganese TRIP steel contained fine equiaxed ferrite and austenite grains. Austenite also has multiple morphologies in first-generation multiphase TRIP steels but can be surrounded by softer ferrite grains, bainite, and in some cases, martensite [26–29]. The retained austenite has an equiaxed morphology in the medium manganese steel and is also surrounded by ferrite like much of the austenite in previous-generation intercritically annealed multiphase TRIP steels, but the amount of retained austenite is much greater, and the ferrite grain size is much finer in the medium manganese steel. Additionally, the austenite in medium manganese TRIP steels is stabilized by substantial manganese partitioning [30,31].

With respect to the influence of temperature on overall deformation behavior, the Q&P and medium manganese TRIP steels also present unique characteristics compared with single-phase austenitic steels and first-generation multiphase TRIP steels. The martensite in Q&P steel has a high dislocation density and many high-angle boundaries [32], and thus has a large athermal strengthening component compared with first-generation multiphase TRIP steels. A large athermal strengthening component is expected to result in low flow stress temperature sensitivity [33]. In contrast, the ferrite in medium manganese TRIP steel has a relatively low dislocation density and athermal strengthening component, likely leading to a higher temperature sensitivity of flow stress [33,34]. Medium manganese TRIP steels often exhibit a distinct upper yield point followed by Lüders band behavior and then work hardening characterized by serrations and Portevin–Le Châtelier (PLC) bands [35,36]. The serrated flow behavior may be indicative of dynamic strain aging (DSA) potentially due to C-Mn point defect complexes interacting with stacking faults in the austenite [35,37,38], although in some cases, serrated flow has been attributed to the austenite-to-martensite transformation [39,40]. Studies on the Lüders and PLC bands exhibited by medium manganese TRIP steels show that strain-induced austenite-to-martensite transformation occurs within the bands where there is high localized plastic deformation [36,40,41]. A study by Field and Van Aken examined DSA in experimental medium manganese (10–14 wt.%) TRIP steels and reported activation energies for DSA that support the following mechanisms that will be considered in this paper: interaction of C-Mn defect complexes with dislocations in austenite and nitrogen pinning of dislocations in ferrite [35]. Overall, the temperature sensitivity of deformation behavior is impacted by multiple mechanisms beyond just the retained austenite-to-martensite transformation.

In this paper, tensile test data from tests at  $-10$  to  $85$  °C for a Q&P steel and  $-10$  to  $115$  °C for a medium manganese TRIP steel are presented and compared with respect to temperature sensitivity of flow stress, austenite stability, and deformation mechanisms. Based on the preceding review of the field, this work contributes new information on austenite stability and tensile deformation behavior of third-generation AHSS within a temperature range of importance for the automotive industry.

## 2. Materials and Methods

The chemical compositions of the Q&P steel, designated QP3Mn, and the medium manganese TRIP steel, designated TRIP7Mn, are provided in Table 1. The QP3Mn steel was obtained as a laboratory heat that was cold-rolled 50% to a thickness of 1.1 mm. The prior processing before the cold-rolling step is described elsewhere [8]. The QP3Mn machined tensile specimens were subjected to quenching and partitioning heat treatments based on the work of De Moor et al. on an alloy with similar amounts of carbon, manganese, and silicon [42]. The samples were held at an austenitizing temperature of  $830$  °C for 120 s, quenched to  $180$  °C (it took 10 s to reach  $180$  °C), and held at a partitioning temperature of  $400$  °C for 10 s. Salt pots were used for all three processing steps, and three tensile specimens were heat-treated at a time. The TRIP7Mn material came from an industrial trial, and the processing steps that can be described are provided in more detail elsewhere [43]. The alloy was hot-rolled, batch-annealed, cold-rolled to a final thickness of 1.4 mm, and finally intercritically batch-annealed. The TRIP7Mn steel was tested in the as-received condition.

**Table 1.** Sheet steel chemical compositions (wt.%).

Alloy	C	Mn	Si	Al	N	S	P
QP3Mn	0.28	2.56	1.56	0.049	0.0037	0.002	0.01
TRIP7Mn	0.14	7.14	0.23	0.056	0.012	0.002	0.007

The electron backscatter diffraction (EBSD) specimens were polished through various standard grinding and polishing steps; final polishing was performed using a  $1$   $\mu\text{m}$  diamond slurry and then  $0.02$   $\mu\text{m}$  colloidal silica on a vibratory polisher for 4 h. EBSD patterns were collected with TSL OIM<sup>TM</sup> Data Collection 7 software using a  $0.03$ – $0.05$   $\mu\text{m}$  step size at a 20 keV operating voltage, and TSL OIM<sup>TM</sup> Analysis 7 software was used to analyze the patterns. A JEOL JSM-7000F FE-SEM and a FEI Helios NanoLab 600i FIB-SEM were used for EBSD. For the TRIP7Mn grain size measurements, the data set was analyzed using neighbor phase correlation with a 0.1 minimum confidence index.

X-ray diffraction (XRD) was performed on as-heat-treated specimens and on tensile specimens interrupted at various strain levels. A separate tensile test was performed for each plastic strain level, and the XRD sample consisted of the deformed gage section. The specimens were lightly ground with 400 and 600 SiC paper to remove the surface oxide layer. Samples were thinned in 10 parts deionized water, 10 parts 30% hydrogen peroxide, and 1 part 48% hydrofluoric acid for 15 to 20 min. The XRD scans were performed with a Philips X'pert X-ray diffractometer using nickel-filtered copper  $K\alpha$  radiation with a one-degree incident beam slit, operating at 45 kV and 40 mA, and using an X'celerator detector. Samples oriented with the rolling direction parallel to the X-ray beam were scanned over a 2-theta range of  $40^\circ$ – $105^\circ$  with a 200 s dwell time and  $0.05^\circ$  step size. PANalytical X'Pert HighScore Plus software was used to analyze the raw XRD data. The  $K\alpha_2$  peaks were removed, and the remaining  $K\alpha_1$  peaks were fit using the peak fitting routine called Profit. From the peak fits, the software calculated the integrated intensity (neglecting the background radiation) and position for each peak. The integrated intensities and peak positions were used to calculate the austenite volume fraction with the recommended multiplex comparison method from Jatzcak et al. [44]. Four ferrite peaks, {110}, {200}, {211}, and {220}, and four austenite peaks, {111}, {200}, {220}, and {311}, were used for the calculation.

Figure 1 shows a schematic of the employed tensile specimen geometry [45]. The tensile specimens were machined by wire electrical discharge machining (EDM) with the tensile axis parallel to the rolling direction. To reduce slipping in the grips, 80 grit SiC paper was used to grind a crosshatch pattern into the grip portions of the tensile specimen prior to testing. Tensile specimens deformed at elevated temperature in an oil bath required a pin hole in one of the grip sections.

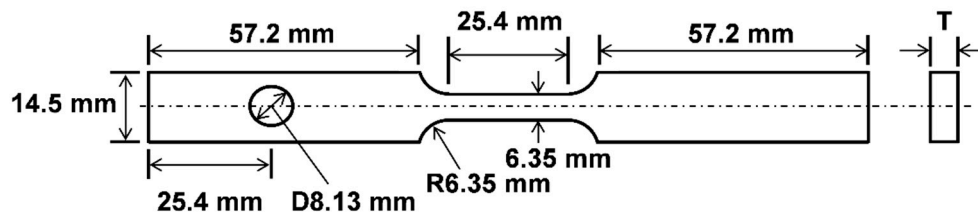


Figure 1. Schematic of tensile specimen geometry.

Tensile testing was performed at room temperature and at  $-10\text{ }^{\circ}\text{C}$  in air on a screw-driven MTS Alliance RT/100 test system at a displacement rate of  $0.0127\text{ mm/s}$ . Three tests were performed to fracture at each temperature. The interrupted tensile tests were performed at each temperature by stopping the tensile test at a selected level of displacement and unloading the specimen. One interrupted tensile test was performed for each reported plastic strain level, and the partially deformed specimen was used for XRD measurements. An MTS  $25.4\text{ mm} + 12.7\text{ mm}/-2.5\text{ mm}$  extensometer was used for the room temperature tests, and a Shepic  $25.4\text{ mm} + 12.7\text{ mm}$  extensometer was used for the tests at  $-10\text{ }^{\circ}\text{C}$ . A compressed air EXAIR<sup>®</sup> Adjustable Spot Cooler with two  $25.4\text{ mm}$  flat nozzles was used to obtain a test temperature of  $-10\text{ }^{\circ}\text{C}$ . The actual test temperatures at the center of the gage section were within  $\pm 2\text{ }^{\circ}\text{C}$  of  $-10\text{ }^{\circ}\text{C}$ , and the temperature at either end of the gage section (near the fillets) was measured to be  $3\text{ }^{\circ}\text{C}$  higher than the temperature in the center of the gage section.

Isothermal elevated temperature tensile tests were performed in Paratherm oil on a screw-driven Instru-Met test system with a Shepic  $25.4\text{ mm} + 12.7\text{ mm}$  extensometer and a displacement rate of  $0.0127\text{ mm/s}$ . The specimens were submerged for at least 3 min prior to testing. Duplicate specimens were tested to fracture at test temperatures of 40, 55, 70, and  $85\text{ }^{\circ}\text{C}$ . Two tensile tests were also conducted to fracture at 100 and  $115\text{ }^{\circ}\text{C}$  for the TRIP7Mn steel. The interrupted tensile tests were performed in the same manner described previously for the tests at room temperature and at  $-10\text{ }^{\circ}\text{C}$ . The actual test temperatures were within  $\pm 1\text{ }^{\circ}\text{C}$  of the target temperature, except for  $40\text{ }^{\circ}\text{C}$  for which the actual test temperatures were within  $\pm 3\text{ }^{\circ}\text{C}$  of the target temperature.

### 3. Results and Discussion

#### 3.1. Microstructure

The QP3Mn and TRIP7Mn microstructures are shown in the EBSD phase maps combined with image quality maps in Figure 2. The QP3Mn microstructure shown in Figure 2a is mostly martensitic with interspersed filmlike austenite and blocky austenite. The observed morphology of the martensite phase is consistent with a lath martensite microstructure expected for this alloy and processing condition. The austenite content measured from the EBSD phase map is 9 vol.%, while the average and corresponding standard deviation of the austenite content measured by XRD from four separate samples is  $14 \pm 1\text{ vol.}\%$ . The austenite content from XRD may be higher than the amount measured using EBSD because the austenite films are poorly resolved with EBSD due to their small thickness dimension. Further, XRD was performed on multiple samples and had a larger sample area than EBSD. The TRIP7Mn microstructure shown in Figure 2b contains equiaxed and interspersed ferrite and austenite grains. Annealing twins are visible in some of the austenite grains. The ferrite grain size is  $1.2 \pm 0.5\text{ }\mu\text{m}$ , and the austenite grain size is  $0.8 \pm 0.3\text{ }\mu\text{m}$ . The

austenite content measured from the EBSD phase map is 43 vol.%, and the average and corresponding standard deviation of the austenite content measured by XRD from four separate samples is  $39 \pm 2$  vol.%. The greater amount of austenite and the larger equiaxed grains are contributing factors to the better agreement between EBSD and XRD for the medium Mn TRIP steel microstructure versus the Q&P microstructure.

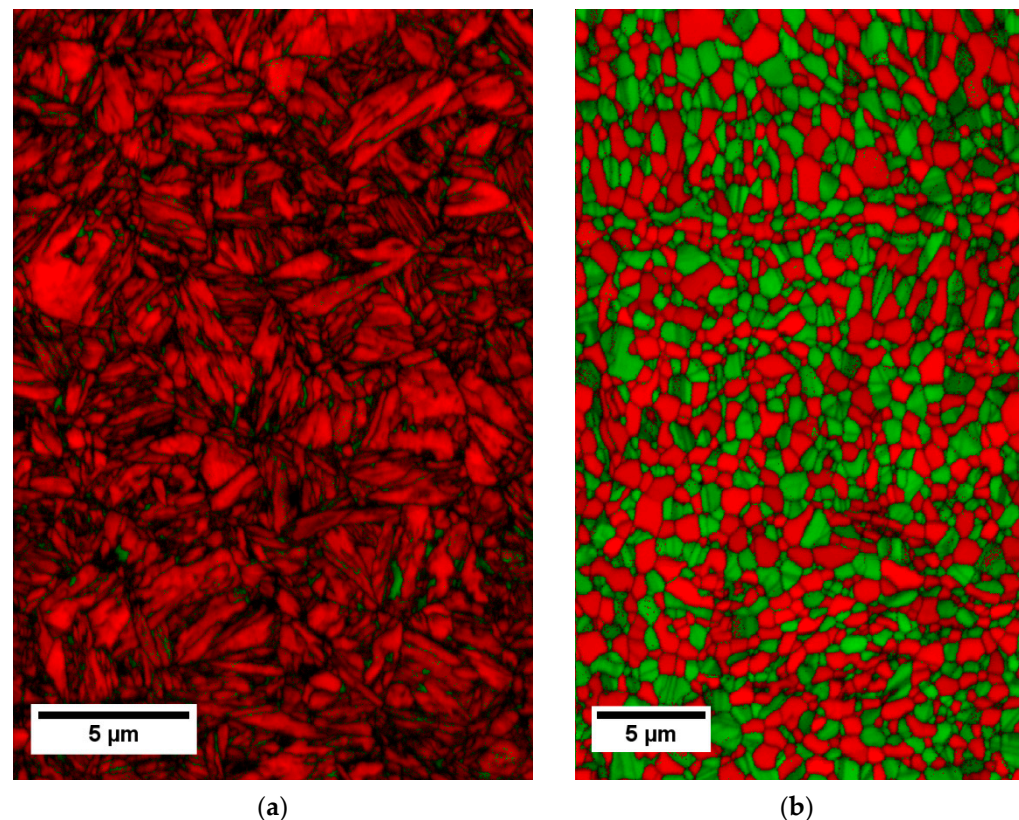


**Figure 2.** Combined EBSD phase map and image quality map showing the as-processed microstructures of (a) QP3Mn and (b) TRIP7Mn. Red indicates ferrite/martensite and green indicates austenite.

### 3.2. Tensile Deformation Behavior and Properties

Figure 3a shows example engineering tensile stress–strain curves for QP3Mn at temperatures between  $-10$  and  $85$  °C. All of the flow curves exhibit continuous yielding, UTS values between 1500 and 1650 MPa, and total elongation (TE) between 10% and 15%. The flow curves are very similar in terms of yielding and work hardening behavior. The results at higher temperature exhibit somewhat less uniform elongation (UE). During necking at 70 and 85 °C, there are possible serrations in the flow curve that appear low in magnitude and frequency, as shown by the zoomed-in stress–strain plot in Figure 3a. Figure 3b shows work hardening rate ( $d\sigma/d\varepsilon$ ) calculated from true stress and strain as a function of true plastic strain for the same test conditions shown in Figure 3a. Most of the work hardening in the QP3Mn occurs at low strains near yielding. The martensitic matrix likely dominates the low strain work hardening behavior as the observed work hardening behavior is similar to that exhibited by an as-quenched or lightly tempered lath martensitic alloy [46–48]. The TRIP effect likely contributes to the work hardening behavior at higher strains, as discussed later. The work hardening rate at  $-10$  °C is distinctly higher than the work hardening rates observed at elevated test temperatures, which results in higher flow stress values at larger strains. Up to approximately 4% strain, the work hardening rates are similar for tests at 22 to 85 °C, but above 4% strain, the work hardening rate decreases more rapidly with increasing strain for the 70 and 85 °C tests compared with the tests at lower temperatures, which results in lower UE at 70 and 85 °C. This change in work hardening behavior is discussed further in the section relating tensile properties to microstructure.

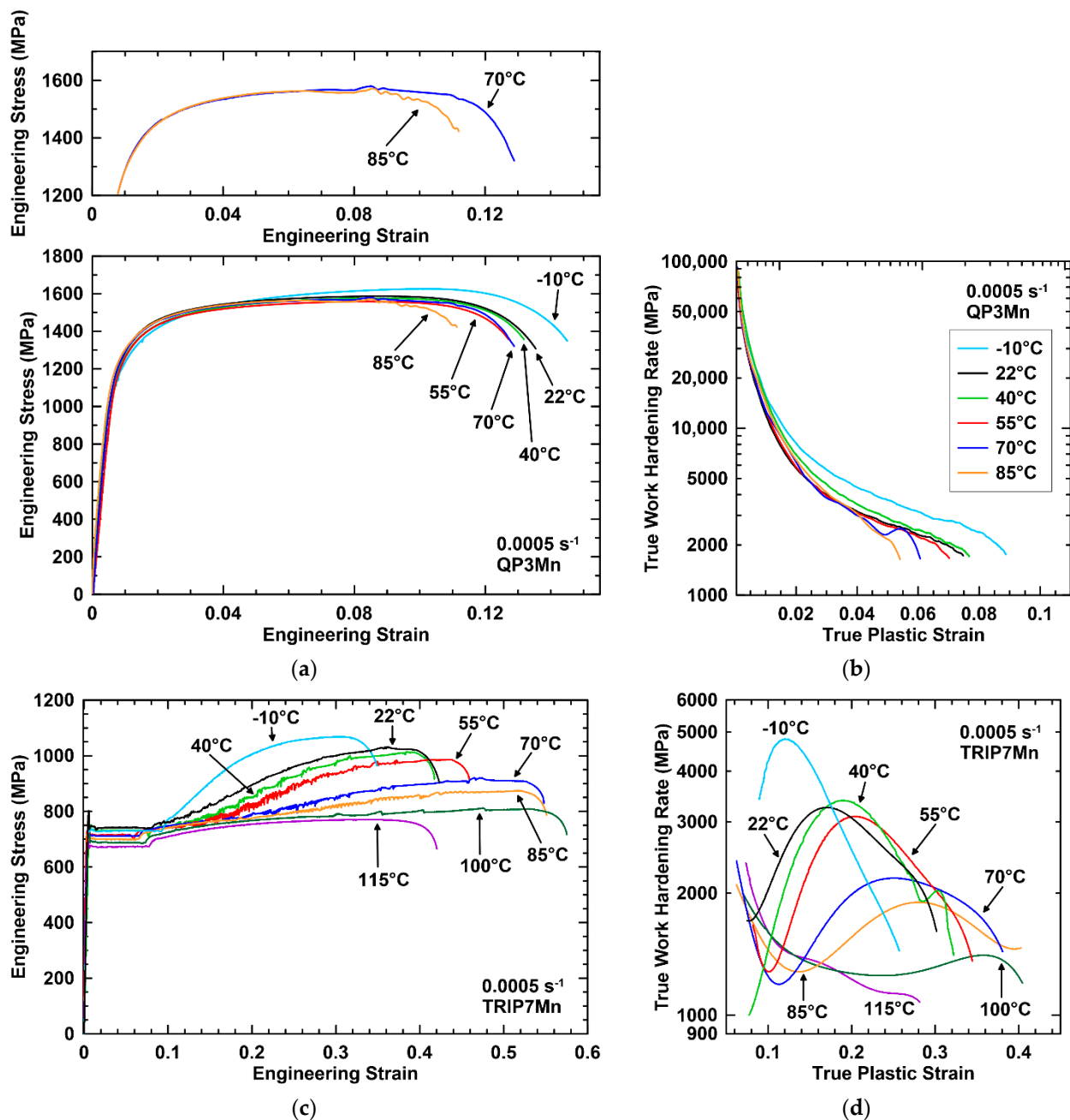


**Figure 3.** Representative engineering stress–strain curves from tests at  $0.0005 \text{ s}^{-1}$  and various temperatures for (a) QP3Mn and (c) TRIP7Mn. Serrated flow behavior during necking is shown by the zoomed-in stress–strain plot for QP3Mn. Work hardening rate ( $d\sigma/d\varepsilon$ ) as a function of strain from tests at  $0.0005 \text{ s}^{-1}$  and various temperatures for (b) QP3Mn and (d) TRIP7Mn. Work hardening rate was calculated from a smoothed true stress–strain curve obtained by a polynomial fit to the plastic deformation region between yield point elongation (YPE)/yielding and necking.

Example engineering stress–strain curves for TRIP7Mn at temperatures between  $-10$  and  $115^\circ\text{C}$  are shown in Figure 3c. All of the curves exhibit distinct upper and lower yield points with yield point elongation (YPE) greater than 5% strain. TEM observations during YPE of a similar 7 wt.% Mn TRIP steel showed that the ferrite has a very low initial dislocation density after annealing, and it is likely that the ferrite experiences static strain aging at room temperature, which both contribute to yield point elongation by the nucleation and propagation of Lüders bands [34]. Additionally, fine grain size (around  $1 \mu\text{m}$ ) is associated with a high Lüders strain in steel alloys with ferrite–cementite, ferrite–austenite, and fully austenitic microstructures [49–51]. Stress-induced austenite-to-martensite transformation

can also contribute to a distinct yield point and stress plateau [18]. Factors contributing to YPE in TRIP7Mn are discussed in more detail later.

In the temperature range of 22 to 100 °C, TRIP7Mn undergoes discontinuous plastic deformation beyond YPE, giving the appearance of serrations in the flow curve. The flow curve is also characterized by distinct steplike segments, which likely correspond to the motion of PLC bands from one end of the gage length to the other end [52,53]. The serrations increase in prominence at 40 and 55 °C. The fine serrations decrease in intensity, and the steplike appearance is reduced as the flow curves become flatter and smoother as temperature increases through 70 and 85 °C. By 100 °C, the fine serrations disappear, but the curve still contains distinct nearly linear segments that are bound by abrupt load increases and drops. At 115 °C, there are no serrations or excursions in the flow curve, and there is very little work hardening compared with the lower test temperatures. The flow curve also does not exhibit serrations at −10 °C. The trend of the serrations increasing and then decreasing in magnitude and frequency with increasing temperature was similarly observed for austenitic Hadfield steel in the temperature range of −10 to 200 °C [37].

The serrated flow behavior may be due to DSA caused by C-Mn point defect complexes in the austenite that reorient within a stacking fault and pin the partial dislocations [37,38]. The critical strain at which the serrations begin increases with increasing temperature for TRIP7Mn. The serrations begin immediately following YPE at 22 °C but do not begin until 30% strain at 100 °C. The increase in the critical strain with increasing temperature for TRIP7Mn may be due to an increase in stacking fault energy (SFE) with increasing temperature, as previously reported for the onset of DSA in austenitic twinning-induced plasticity (TWIP) steel due to C-Mn point defect complexes in the austenite [38]. As noted in the introduction, nitrogen pinning of dislocations in ferrite is another potential mechanism for DSA in medium manganese TRIP steel [35] and may be a plausible mechanism for TRIP7Mn. Most of the as-processed TRIP7Mn microstructure is ferrite (57% by EBSD or 61% by XRD), and bulk nitrogen was measured at 120 ppm. However, the partitioning of the nitrogen between ferrite and austenite is not known.

Overall, Figure 3c shows that with increasing test temperature, there are decreases in the lower yield strength (YS), flow stress between the YPE region and up to UTS, work hardening rate, and UTS. The UE and TE correspondingly increase with increasing temperature, except at the highest temperature of 115 °C. The trends in serrated flow behavior and mechanical behavior with respect to test temperature for TRIP7Mn are similar to the trends observed for a steel with the same chemical composition that was intercritically annealed for various times to achieve different ferrite and austenite grain sizes [43]. Comparing TRIP7Mn with QP3Mn, increasing temperature causes a greater decrease in work hardening rates and UTS for TRIP7Mn than for QP3Mn. The two alloys also exhibit opposite behaviors with respect to the change in elongation values with increasing temperature.

The TRIP7Mn work hardening rates ( $d\sigma/d\varepsilon$ ) were calculated as a function of true plastic strain from smoothed stress–strain curves (meaning that serrations in the stress–strain curve were not considered) for all test temperatures. Curve smoothing was accomplished by fitting a sixth-order polynomial to the true stress and strain data in the region of plastic deformation from the end of YPE up to the onset of necking. The work hardening rate versus true plastic strain data in Figure 3d show that test temperature has a major impact on work hardening behavior for the TRIP7Mn steel. With increasing true plastic strain beyond about 10% strain, the work hardening rate increases to a maximum for all test temperatures except 115 °C. This behavior is largely due to the introduction of martensite into the ferrite–austenite microstructure during straining [54]. The peak in work hardening rate occurs at 12% strain at −10 °C and occurs at greater values of true plastic strain as temperature increases with the work hardening rate peak occurring at 36% strain at 100 °C. The prolonged work hardening at higher strains with increasing test temperature contributes to the increase in UE with increasing test temperature. The maximum in the work hardening rate (beyond 10% true plastic strain) also generally decreases with increasing temperature

with the peak at  $-10\text{ }^{\circ}\text{C}$  near 5000 MPa and the peak at  $100\text{ }^{\circ}\text{C}$  below 1500 MPa. At  $115\text{ }^{\circ}\text{C}$ , the work hardening rate decreases monotonically with increasing true plastic strain, consistent with the lower UE and ductility at this temperature.

### 3.3. Retained Austenite-to-Martensite Transformation Behavior

The retained austenite volume fraction versus plastic engineering strain from tensile tests performed from  $-10$  to  $85\text{ }^{\circ}\text{C}$  for QP3Mn is shown in Figure 4a. For all test temperatures, the retained austenite fraction decreases with increasing strain. As expected, the austenite-to-martensite transformation rate decreases with increasing test temperature (i.e., austenite becomes more stable with increasing test temperature). The greatest amount of austenite transformation occurs at  $-10\text{ }^{\circ}\text{C}$ , which may contribute to the higher work hardening rate observed at  $-10\text{ }^{\circ}\text{C}$  compared with the higher test temperatures. However, increased austenite stability at higher temperatures appears to have a much smaller impact on work hardening rates. The austenite-to-martensite transformation behavior is similar at  $70$  and  $85\text{ }^{\circ}\text{C}$  with high austenite stability up to 4% strain and more than half of the austenite remaining at the onset of necking. As previously noted, there is a significant drop in work hardening rate at  $70$  and  $85\text{ }^{\circ}\text{C}$  above 4% strain that is not observed in the lower temperature conditions until higher strains. This decrease in work hardening rate is attributed to the higher austenite stability at these temperatures.

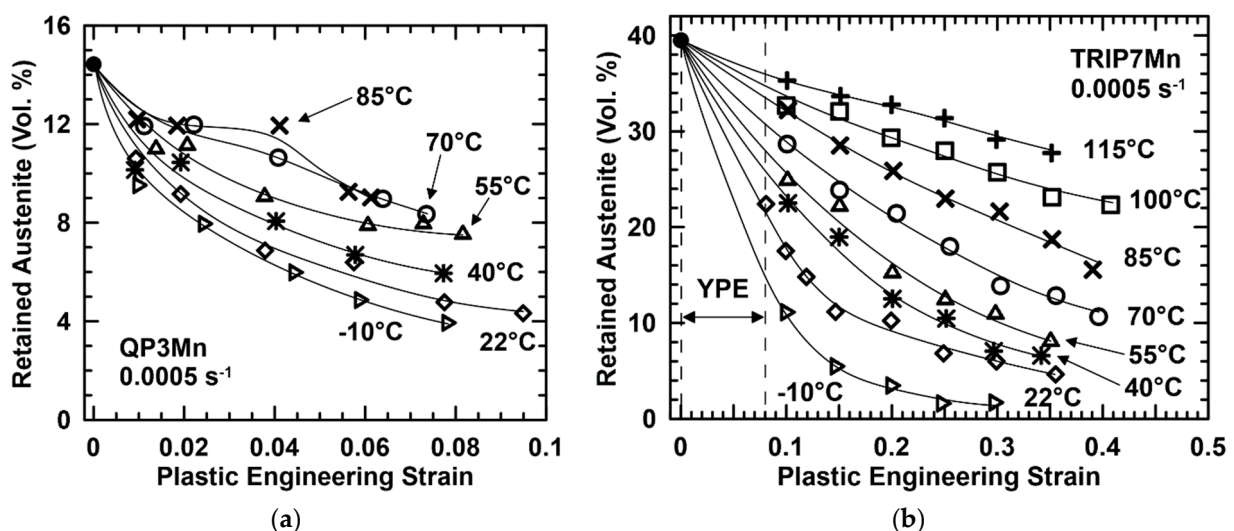


**Figure 4.** Austenite volume fraction versus plastic strain from tests at  $0.0005\text{ s}^{-1}$  and various temperatures for (a) QP3Mn and (b) TRIP7Mn.

Retained austenite volume fraction versus plastic engineering strain from tensile tests at temperatures in the range of  $-10$  to  $115\text{ }^{\circ}\text{C}$  for TRIP7Mn is shown in Figure 4b. All of the austenite measurements were performed beyond YPE. At  $22\text{ }^{\circ}\text{C}$ , the retained austenite amount drops from 40 vol.% in the as-received material to 22 vol.% post-YPE at 8% plastic strain. Lüders band deformation behavior has been linked to a stress-assisted transformation in other alloy systems, such as NiTi [55,56], and there is a significant amount of transformation during this regime for the TRIP7Mn steel. However, it has also been suggested that local plastic deformation in a Lüders band can lead to strain-induced transformation to martensite in ultrafine grain medium Mn TRIP steel [57]. As temperature increases, the amount of austenite that transforms during YPE decreases, which is consistent with the expected thermal stability of austenite for either a strain-induced or stress-assisted transformation. The possibility of stress-assisted transformation is considered further in the section linking microstructure and tensile behavior.

The strain-induced transformation of austenite to martensite beyond YPE contributes to a high work hardening rate and high ductility [58]. The TRIP7Mn retained austenite

stability is very temperature sensitive in the examined temperature range with austenite becoming more stable with increasing temperature. For example, the amount of austenite remaining at approximately 30% plastic strain is 2 vol.% at  $-10\text{ }^{\circ}\text{C}$  and 29 vol.% at  $115\text{ }^{\circ}\text{C}$ . In the context of the work hardening rate curves in Figure 3d, the observed peak in work hardening rate (beyond 10% plastic strain) decreases in magnitude and shifts to higher strain with increasing temperature as the austenite-to-martensite transformation rate decreases. Therefore, the decrease in the austenite-to-martensite transformation rate with increasing temperature contributes to a reduction in work hardening rate and UTS.

Olson and Cohen developed a mechanism-based model for the strain-induced austenite-to-martensite transformation based on the concept that shear band intersections are the dominant nucleation sites for martensite [25]. The model is expressed by Equation (1), where  $f_{\alpha'}$  is the volume fraction of transformed martensite,  $\varepsilon$  is true plastic strain,  $\alpha$  is a parameter that reflects the rate of shear band formation,  $\beta$  is a parameter related to the probability of forming martensite nuclei at a shear band intersection, and  $n$  is a fixed exponent term that relates to the number of intersections in the austenite. Both  $\alpha$  and  $\beta$  depend on composition and temperature. The use of macroscopic true strain in the model for steels containing ferrite or martensite ignores potential strain partitioning effects in multiphase microstructures. While this is an important consideration for applying the model to the transformation behavior of austenite-containing multiphase microstructures, the model fits experimental data for first-generation TRIP steels as well as for some medium Mn TRIP and Q&P steels [43,58–61].

$$f_{\alpha'} = 1 - \exp(-\beta \cdot (1 - \exp(-\alpha\varepsilon))^n) \quad (1)$$

Nonlinear least squares regression was used to fit the Olson–Cohen model, given in Equation (1), to the fraction of transformed martensite (calculated from the retained austenite phase fraction measurements) at various amounts of plastic true strain for each test temperature. A value of  $n$  equal to 2 provided the closest fit between the Olson–Cohen model and the experimental data (among  $n$  values greater than or equal to 2) for both steels. The value of  $n$  equal to 2 is taken to be a lower bound based on Olson and Cohen's derivation using the assumption that the shear bands are randomly oriented with a length equal to the austenite grain size [25]. The experimental data and fitted model curves are shown in Figure 5a for QP3Mn and Figure 5c for TRIP7Mn. The model curves agree well with the experimental data for TRIP7Mn, while the QP3Mn curve fits are somewhat poorer for some of the data.

For QP3Mn, there is a fraction of austenite that immediately transforms, by 1% plastic strain, followed by more gradual austenite transformation with increasing strain. The substantial amount of martensite formed, relative to the trend for the other tensile strains, caused a poor fit of the model to the data, especially at  $70$  and  $85\text{ }^{\circ}\text{C}$ . Therefore, the model is fit to the data at 2% and greater strains for all temperatures, and the resulting model curve fits, shown in Figure 5a, agree with most of the data for temperatures in the range of  $-10$  to  $70\text{ }^{\circ}\text{C}$ . The relatively large fraction of austenite that transforms by 1% plastic strain may indicate two different populations of retained austenite with different stabilities. For example, blocky austenite has been shown to be less stable than film austenite [26,28,29,62], and in a study on a QP980 grade, the extent of austenite-to-martensite transformation differed between blocky and film austenite as test temperature increased [63]. In the QP3Mn steel, the low strain transformation behavior may be dominated by the less stable blocky retained austenite, while the higher strain behavior may be more indicative of thin film austenite. Alternatively, the high rate of initial transformation could potentially be due to stress-assisted austenite transformation at low strains, which could cause a poor fit of the Olson–Cohen model that was developed for strain-induced austenite transformation.

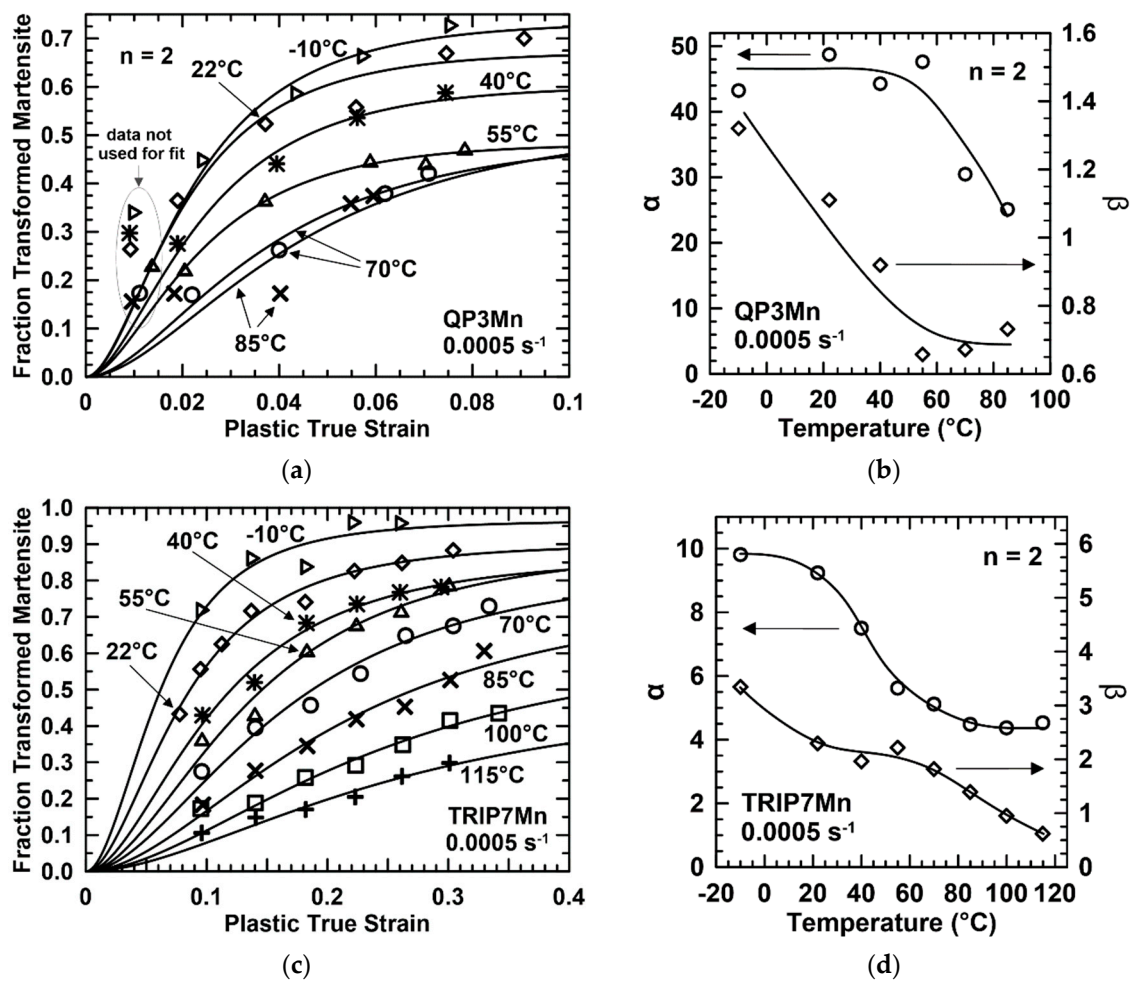


**Figure 5.** Fraction of transformed martensite versus plastic strain at various test temperatures ( $0.0005 \text{ s}^{-1}$  strain rate) for (a) QP3Mn and (c) TRIP7Mn. The points are experimental data, and the curves are the Olson–Cohen model fits. For QP3Mn, data at 2% and greater strain were used for model fits. Olson–Cohen model parameters  $\alpha$  and  $\beta$  versus temperature with  $n$  equal to 2 for (b) QP3Mn and (d) TRIP7Mn.

The model parameters  $\alpha$  and  $\beta$  are plotted as functions of temperature in Figure 5b for QP3Mn and Figure 5d for TRIP7Mn. The values of  $\alpha$  and  $\beta$  generally decrease with increasing temperature for both steels. The parameter  $\alpha$  depends on stacking fault energy, and the parameter  $\beta$  depends on the chemical driving force for the austenite-to-martensite transformation; both parameters are expected to decrease with increasing temperature as the strain-induced austenite-to-martensite transformation rate decreases [25]. The calculated QP3Mn  $\alpha$  and  $\beta$  parameters at room temperature are similar to those determined by De Moor et al. for a 0.17C-1.65Mn-0.38Si-1.11Al-0.08P (wt.%) steel that was subjected to Q&P heat treatments with different partitioning temperatures (PT) to produce different amounts of austenite in the final microstructure [61]. The TRIP7Mn  $\alpha$  and  $\beta$  parameters are also consistent with values obtained at room and elevated temperatures in other studies of 7 wt.% Mn TRIP steels with similar initial microstructures [43,58]. In the temperature range of  $-10$  to  $85 \text{ }^\circ\text{C}$ ,  $\alpha$  is greater for QP3Mn and  $\beta$  is greater for TRIP7Mn. These model results suggest that QP3Mn exhibits a greater rate of shear band formation and a lower probability of forming martensite nuclei. These results may imply differences in relative stacking fault energy and chemical driving force for transformation between the two alloys. Alternatively, there could be austenite morphology effects on the probability of forming martensite at shear band intersections.

### 3.4. Correlation of Tensile Mechanical Properties with Microstructure

The dependence of UTS and 0.2% offset YS on test temperature for QP3Mn, plotted in Figure 6a, shows that there is no significant effect of temperature on the YS or UTS for temperatures between 22 and 85 °C. There is also no significant difference in YS between −10 and 22 °C within the scatter of the data, but there is a small decrease in UTS between −10 and 22 °C, which arises due to the differences in work hardening behavior as shown in Figure 3b. The yielding behavior may reflect martensite with very low temperature sensitivity, since the initial microstructure is approximately 86% martensite. Any effect of temperature on yielding of the austenite appears to have a negligible contribution to the overall flow stress. At UTS, a fraction of the retained austenite has transformed to martensite at all temperatures, but the increase in austenite stability with increasing temperature (see Figure 4a) does not have a clear impact on UTS. Thus, the flow stress of QP3Mn is dominated by the mostly martensitic initial microstructure. Although the martensite has undergone a short partitioning heat treatment, which would reduce the carbon content and likely result in some recovery, the martensite deformation behavior is expected to be dominated by long-range dislocation interactions, which can include packet boundaries, precipitates, and dislocation tangles [64]. Long-range dislocation interactions contribute to the athermal component of flow stress, while the thermal component of flow stress arises from short-range dislocation obstacles, such as the Peierls–Nabarro stress and dislocation forests [7,33]. Wang et al. recently quantified the athermal and thermal components of flow stress in quenched and tempered steels [65]. For a steel similar in chemical composition (0.25C-2.42Mn-1.44Si-0.01Al mass%) to the current work that was quenched and then tempered at 400 °C for 5 min, the athermal component accounted for approximately 75% of flow stress [65]. For QP3Mn, temperature-sensitive short-range dislocation barriers do not appear to have a significant impact on flow stress for two reasons: (1) their contribution to flow stress is very small compared with long-range barriers, and (2) the test temperature range is small (i.e., approximately 95 °C), which amounts to a small increase in the thermally dependent component of flow stress. The magnitudes of the contributions of the athermal and thermal components of flow stress are different between QP3Mn, with a martensite matrix, and TRIP7Mn, with an equiaxed ferrite matrix. This difference is a factor contributing to the differences in temperature sensitivity of tensile properties, which will be discussed further in the context of the TRIP7Mn tensile behavior.

The dependence of UE and TE on test temperature for QP3Mn is shown in Figure 6b. The UE decreases slightly with increasing temperature for a total average decrease of 3% strain from −10 to 85 °C. Most of the UE decline occurs between −10 and 55 °C, and the UE is similar at 70 and 85 °C. Austenite stability increases with increasing temperature up to 70 °C (see Figure 4a), and correspondingly, UE decreases. The austenite-to-martensite transformation rates are nearly the same at 70 and 85 °C, and the elongation data are also very close between 70 and 85 °C. The TE also declines on average by 3% strain from −10 to 55 °C. The decreases in UE and TE with increasing temperature are consistent with previously published behavior of a QP980 grade [24]. For QP3Mn, the TE appears to increase at temperatures above 55 °C for some of the test specimens, implying an increase in post-uniform elongation. The increase in TE at higher temperatures coincides with the appearance of serrations in the flow curves. The association of the serrations with enhanced post-uniform elongation suggests a mechanism that increases plasticity, but the mechanism is unknown.

The upper and lower YS for TRIP7Mn are plotted versus temperature in Figure 6c. There is a slight decrease in both the upper and lower YS from 22 to −10 °C. These observations are consistent with the possibility of stress-assisted austenite transformation associated with YPE, as stress-assisted austenite transformation is favored at lower temperature and causes a decrease in YS [18,66,67]. While there is evidence of stress-induced transformation at −10 °C, it is not entirely clear whether the austenite transformation is stress-assisted or strain-induced at all test temperatures.

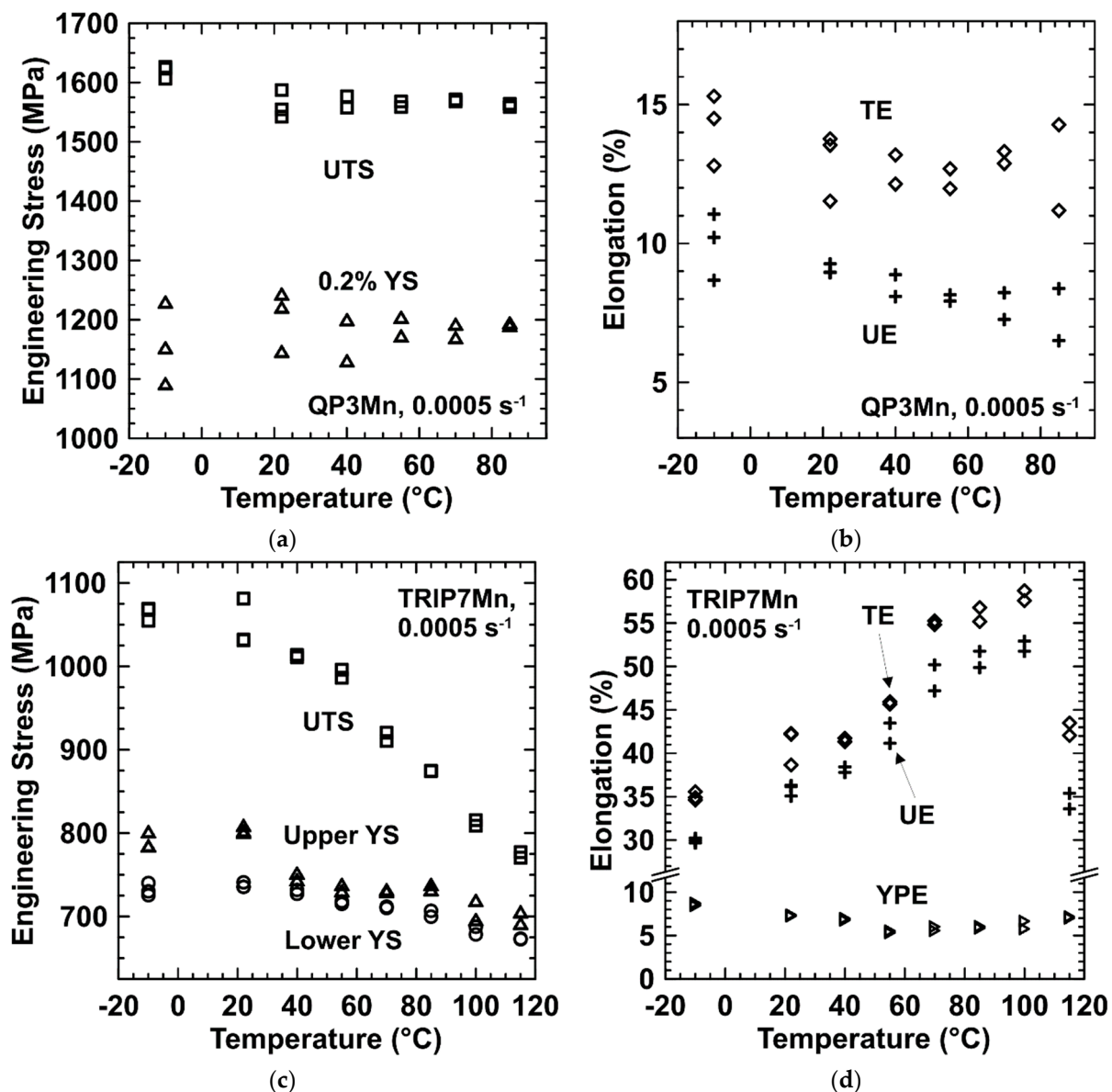


**Figure 6.** Tensile mechanical properties versus temperature from replicate tests at 0.0005 s<sup>-1</sup>. (a) QP3Mn 0.2% YS and UTS; (b) QP3Mn UE and TE; (c) TRIP7Mn lower YS, upper YS, and UTS; and (d) TRIP7Mn YPE, UE, and TE.

Both the upper and lower YS decrease with increasing temperature above 22 °C. Increasing temperature provides an increased thermal contribution that lowers the stress necessary for dislocations to overcome short-range barriers, thereby decreasing flow stress [33]. The thermal contribution to flow stress is smaller in austenite with a face-centered cubic lattice than ferrite with a body-centered cubic lattice, and ferrite is the majority of the microstructure. Thus, it is interpreted that ferrite has greater influence on the decrease in YS with increasing temperature above 22 °C. The upper and lower YS of TRIP7Mn exhibit substantial temperature sensitivity in contrast to QP3Mn. This difference in behavior is due to the large amount of ferrite in the TRIP7Mn microstructure compared with the mostly martensitic QP3Mn microstructure. There are significantly fewer long-range dislocation interactions in ferrite than martensite, enhancing the influence of temperature-sensitive short-range barriers on the flow stress in ferrite.

There is a much greater effect of temperature on UTS than YS in TRIP7Mn between 10 and 115 °C, as shown by the UTS versus temperature data in Figure 6c. The average UTS decreases with increasing temperature by 290 MPa over the entire temperature range, largely due to a decrease in work hardening. Multiple factors affect the work hardening

and UTS behavior. There is a small contribution from the addition of thermal energy that assists dislocations in overcoming short-range barriers. However, the change in serrated flow behavior and the stabilization of austenite with increasing temperature have the biggest influence. As shown in Figure 4b, temperature strongly affects austenite stability in the examined temperature range, which in turn contributes to a decrease in work hardening with increasing temperature. While DSA would be expected to cause a peak in UTS in the range of conditions where serrated flow is observed [37], this effect is overwhelmed by the influence of austenite stability. For example, no serrations occur at  $-10\text{ }^{\circ}\text{C}$  and serrations are present at  $22\text{ }^{\circ}\text{C}$ , but the increase in austenite stability with increasing temperature leads to a slight decrease in average UTS of 16 MPa between  $-10$  and  $22\text{ }^{\circ}\text{C}$ . At higher temperatures, a decrease in DSA combined with an increase in austenite stability contributes to larger UTS decreases (e.g., the average UTS drops by 62 MPa between 85 and  $100\text{ }^{\circ}\text{C}$ ). Temperature-dependent austenite stability has a greater effect on TRIP7Mn compared with QP3Mn because there is substantially more deformation-induced transformation that occurs in the TRIP7Mn alloy.

Temperature has a small effect on the YPE of TRIP7Mn, as shown in Figure 6d. The YPE decreases by 3% strain between  $-10$  and  $55\text{ }^{\circ}\text{C}$  and increases by less than 2% strain between  $55$  and  $115\text{ }^{\circ}\text{C}$ . A greater amount of austenite transformation at low temperatures could be a factor contributing to the decrease in YPE with increasing temperature up to  $55\text{ }^{\circ}\text{C}$ . For example, the room temperature test was interrupted immediately at the end of YPE at which point 17 vol.% austenite had transformed. According to a theoretical calculation of elongation due to the austenite-to-martensite transformation alone, transformation of 17 vol.% austenite-to-martensite could produce a maximum of about 2.6% elongation [68]. Austenite phase fraction was not measured immediately at the end of YPE at the other test temperatures, but there was a 14 vol.% difference in austenite at 10% plastic strain between  $-10$  and  $55\text{ }^{\circ}\text{C}$ , suggesting that differences in low strain austenite stability could affect YPE. However, YPE increases above  $55\text{ }^{\circ}\text{C}$  despite the higher austenite stability, indicating that other factors aside from austenite stability affect YPE behavior. At room temperature, austenite transformation would only account for roughly one-third of the YPE, according to theoretical calculation, and grain size likely has a greater effect on the extent of YPE. In a study by Gibbs et al. on a 7 wt.% Mn TRIP steel, YPE decreased substantially with increasing annealing temperature due to increasing grain size even though the amount of austenite transformation during YPE increased significantly [58]. A similar observation was also made by Zhang et al. on a 7 wt.% Mn TRIP steel [43]. In a fine grain low-carbon steel with no austenite-to-martensite transformation, YPE decreased by more than 50% between  $-44$  and  $118\text{ }^{\circ}\text{C}$  (decrease was gradual with increasing temperature) at  $0.0003\text{ s}^{-1}$  [69]. Therefore, changes in austenite stability are not necessary to explain the decrease in YPE as temperature increases. However, the slight increase in YPE above  $55\text{ }^{\circ}\text{C}$  observed for TRIP7Mn indicates that other factors besides fine grain size and austenite stability can affect YPE.

The UE and TE of TRIP7Mn increase in tandem with increasing temperature up to  $100\text{ }^{\circ}\text{C}$ , as shown in Figure 6d. This increase in ductility is attributed to the decrease in both yield strength and low strain work hardening rate (between approximately 0.1 and 0.2 true plastic strain) as temperature increases. Both the yield strength and low strain work hardening rate are critical factors influencing UE [70,71]. Since the formation of martensite is delayed to higher strains with increasing temperature, the resulting work hardening rate at higher strains helps delay instability. However, between  $100$  and  $115\text{ }^{\circ}\text{C}$ , the UE and TE both decrease by over 15% strain, which is consistent with the continuous drop in work hardening rate with strain at  $115\text{ }^{\circ}\text{C}$ , as opposed to the increases at intermediate strains observed in the other conditions. Low work hardening is associated with highly stable austenite in ferrite–austenite steels [49,58]. Aside from austenite stability differences, there is a transition from serrated plastic flow at  $100\text{ }^{\circ}\text{C}$  to continuous plastic flow at  $115\text{ }^{\circ}\text{C}$ . The disappearance of the serrations in the flow curve coincides with the substantial decrease in elongation between  $100$  and  $115\text{ }^{\circ}\text{C}$ . It is interpreted that the decrease in UE at  $115\text{ }^{\circ}\text{C}$  is

due to the loss of DSA contributions to work hardening, thus resulting in instability at a lower strain.

#### 4. Conclusions

The effects of temperature on the strain-induced austenite-to-martensite transformation rate and the tensile mechanical properties of a medium Mn TRIP and a high strength Q&P steel were examined. For TRIP7Mn, increasing test temperature (−10 to 115 °C) results in major changes in work hardening, UTS, and elongation that are associated with a significant increase in austenite stability and the occurrence of serrated plastic flow in the range of 22 to 100 °C. For QP3Mn, increasing test temperature (−10 to 85 °C) results in very little change in YS and UTS, while the UE and TE decrease slightly. Austenite stability increases by a small amount with increasing temperature in the Q&P steel impacting ductility. The conclusions from this work are as follows:

- The effects of temperature on austenite stability and tensile deformation behavior are greater in medium Mn TRIP steel than Q&P steel due to the larger initial volume fraction of austenite, temperature-sensitive DSA, and equiaxed ferrite in the microstructure (due to the contribution of short-range thermal dislocation barriers to flow behavior). The tensile mechanical properties of Q&P steel have low temperature sensitivity due to the mostly martensitic microstructure (more long-range athermal dislocation interactions controlling flow behavior).
- Increasing temperature causes a substantial decrease in the low strain work hardening rate of medium Mn TRIP, which, combined with decreasing yield strength, contributes to a large increase in UE. In contrast, increasing temperature above room temperature has little or no effect on the work hardening rate of quenched and partitioned steel at most strains. The combination of low temperature sensitivity of YS and work hardening rate leads to the smaller influence of temperature on UE in QP3Mn.
- The strain-induced austenite-to-martensite transformation kinetics are highly temperature sensitive for both medium Mn TRIP and quenched and partitioned steels. The Olson–Cohen model is a good fit to the medium Mn TRIP steel data at all test temperatures, but the Olson–Cohen model does not represent the Q&P steel behavior well at 1% strain for all test temperatures.

**Author Contributions:** Conceptualization, W.A.P., E.D.M., J.G.S., K.O.F.; methodology, W.A.P.; formal analysis, W.A.P.; investigation, W.A.P.; writing—original draft preparation, W.A.P.; writing—review and editing, W.A.P., E.D.M., J.G.S., K.O.F.; supervision, K.O.F.; project administration, J.G.S.; funding acquisition, E.D.M., J.G.S., K.O.F. All authors have read and agreed to the published version of the manuscript.

**Funding:** This research was funded by the Advanced Steel Processing and Products Research Center at Colorado School of Mines. Funding was also provided by the National Science Foundation through CAREER Award No. 0955236.

**Acknowledgments:** The authors wish to acknowledge the support of the industrial sponsors of the Advanced Steel Processing and Products Research Center and thank ArcelorMittal and Baosteel for providing the alloys used in the investigation. Ana Araujo is gratefully acknowledged for her assistance with the EBSD experiments.

**Conflicts of Interest:** Whitney A. Poling is an employee of General Motors. The other authors declare no conflict of interest.

#### References

1. Dykeman, J. Advanced High Strength Steel—Recent Progress, Ongoing Challenges, and Future Opportunities. In Proceedings of the International Symposium on New Developments in Advanced High-Strength Sheet Steels, Vail, CO, USA, 23–27 June 2013; AIST: Warrendale, PA, USA, 2013; pp. 15–28.
2. Belanger, P.J.; Hall, J.N.; Coryell, J.J.; Singh, J.P. Automotive Body Press-Hardened Steel Trends. In Proceedings of the International Symposium on New Developments in Advanced High-Strength Sheet Steels, Vail, CO, USA, 23–27 June 2013; AIST: Warrendale, PA, USA, 2013; pp. 239–250.

3. Keeler, S.; Kimchi, M.; Mooney, P.J. *Advanced High-Strength Steels Application Guidelines Version 6.0*; WorldAutoSteel: Brussels, Belgium, 2017.
4. Horvath, C.D.; Enloe, C.M.; Singh, J.P.; Coryell, J.J. Persistent Challenges to Advanced High-Strength Steel Implementation. In Proceedings of the International Symposium on New Developments in Advanced High-Strength Sheet Steels, Keystone, CO, USA, 30 May–2 June 2017; AIST: Warrendale, PA, USA, 2017; pp. 1–10.
5. De Moor, E.; Gibbs, P.J.; Speer, J.G.; Matlock, D.K.; Schroth, J.G. Strategies for Third-Generation Advanced High Strength Steel Development. *AIST Trans. Iron Steel Technol.* **2010**, *7*, 133–144.
6. Hiermaier, S. *Structures Under Crash and Impact: Continuum Mechanics, Discretization and Experimental Characterization*; Springer Science+Business Media: New York, NY, USA, 2008.
7. Meyers, M.A. *Dynamic Behavior of Materials*; Wiley: Hoboken, NJ, USA, 1994.
8. Poling, W.A. Tensile Deformation of Third Generation Advanced High Strength Sheet Steels Under High Strain Rates. Ph.D. Thesis, Colorado School of Mines, Golden, CO, USA, 2016.
9. Talonen, J.; Hänninen, H.; Nenonen, P.; Pape, G. Effect of Strain Rate on the Strain-Induced  $\gamma \rightarrow \alpha'$ -Martensite Transformation and Mechanical Properties of Austenitic Stainless Steels. *Met. Mater. Trans. A* **2005**, *36*, 421–432. [[CrossRef](#)]
10. Lichtenfeld, J.A.; Van Tyne, C.J.; Mataya, M.C. Effect of strain rate on stress-strain behavior of alloy 309 and 304L austenitic stainless steel. *Met. Mater. Trans. A* **2006**, *37*, 147–161. [[CrossRef](#)]
11. Larour, P.; Verleysen, P.; Dahmen, K.; Bleck, W. Strain Rate Sensitivity of Pre-Strained AISI 301LN2B Metastable Austenitic Stainless Steel. *Steel Res. Int.* **2012**, *84*, 72–88. [[CrossRef](#)]
12. Angel, T. Formation of Martensite in Austenitic Stainless Steel. *J. Iron Steel Inst.* **1954**, *177*, 165–174.
13. Talonen, J.; Hänninen, H. Formation of shear bands and strain-induced martensite during plastic deformation of metastable austenitic stainless steels. *Acta Mater.* **2007**, *55*, 6108–6118. [[CrossRef](#)]
14. Iwamoto, T.; Tsuta, T.; Tomita, Y. Investigation on Deformation Mode Dependence of Strain-Induced Martensitic Transformation in TRIP Steels and Modelling of Transformation Kinetics. *Int. J. Mech. Sci.* **1998**, *40*, 173–182. [[CrossRef](#)]
15. Tsuchida, N.; Morimoto, Y.; Tonan, T.; Shibata, Y.; Fukaura, K.; Ueji, R. Stress-Induced Martensitic Transformation Behaviors at Various Temperatures and Their TRIP Effects in SUS304 Metastable Austenitic Stainless Steel. *ISIJ Int.* **2011**, *51*, 124–129. [[CrossRef](#)]
16. Tsuchida, N.; Yamaguchi, Y.; Morimoto, Y.; Tonan, T.; Takagi, Y.; Ueji, R. Effects of Temperature and Strain Rate on TRIP Effect in SUS301L Metastable Austenitic Stainless Steel. *ISIJ Int.* **2013**, *53*, 1881–1887. [[CrossRef](#)]
17. Hecker, S.S.; Stout, M.G.; Staudhammer, K.P.; Smith, J.L. Effects of Strain State and Strain Rate on Deformation-Induced Transformation in 304 Stainless Steel: Part I. Magnetic Measurements and Mechanical Behavior. *Met. Mater. Trans. A* **1982**, *13*, 619–626. [[CrossRef](#)]
18. Olson, G.B.; Azrin, M. Transformation behavior of TRIP steels. *Met. Mater. Trans. A* **1978**, *9*, 713–721. [[CrossRef](#)]
19. Tsuchida, N.; Kawahata, T.; Ishimaru, E.; Takahashi, A. Effects of Temperature and Strain Rate on Tensile Properties of a Lean Duplex Stainless Steel. *ISIJ Int.* **2014**, *54*, 1971–1977. [[CrossRef](#)]
20. Van Der Zwaag, S.; Zhao, L.; Kruijver, S.O.; Sietsma, J. Thermal and Mechanical Stability of Retained Austenite in Aluminum-containing Multiphase TRIP Steels. *ISIJ Int.* **2002**, *42*, 1565–1570. [[CrossRef](#)]
21. Samek, L.; De Moor, E.; Penning, J.; De Cooman, B.C. Influence of Alloying Elements on the Kinetics of Strain-Induced Martensitic Nucleation in Low-Alloy, Multiphase High-Strength Steels. *Met. Mater. Trans. A* **2006**, *37*, 109–124. [[CrossRef](#)]
22. Berrahmoune, M.; Berveiller, S.; Inal, K.; Moulin, A.; Patoor, E. Analysis of the martensitic transformation at various scales in TRIP steel. *Mater. Sci. Eng. A* **2004**, *378*, 304–307. [[CrossRef](#)]
23. Curtze, S.; Kuokkala, V.-T.; Hokka, M.; Peura, P. Deformation Behavior of TRIP and DP Steels in Tension at Different Temperatures over a Wide Range of Strain Rates. *Mater. Sci. Eng. A* **2009**, *507*, 124–131. [[CrossRef](#)]
24. Coryell, J.; Savic, V.; Hector, L.G.; Mishra, S. *Temperature Effects on the Deformation and Fracture of a Quenched-and-Partitioned Steel*; Technical Paper; SAE International: Warrendale, PA, USA, 2013.
25. Olson, G.B.; Cohen, M. Kinetics of strain-induced martensitic nucleation. *Met. Mater. Trans. A* **1975**, *6*, 791–795. [[CrossRef](#)]
26. Sugimoto, K.; Misu, M.; Kobayashi, M.; Shirasawa, H. Effects of Second Phase Morphology on Retained Austenite on Ductility of TRIP-Aided Dual-Phase Steels. *ISIJ Int.* **1993**, *33*, 775–782. [[CrossRef](#)]
27. Jacques, P.; Delannay, F.; Ladrière, J. On the influence of interactions between phases on the mechanical stability of retained austenite in transformation-induced plasticity multiphase steels. *Met. Mater. Trans. A* **2001**, *32*, 2759–2768. [[CrossRef](#)]
28. Timokhina, I.B.; Hodgson, P.D.; Pereloma, E.V. Effect of Microstructure on the Stability of Retained Austenite in Transformation-Induced-Plasticity Steels. *Met. Mater. Trans. A* **2004**, *35*, 2331–2341. [[CrossRef](#)]
29. Chiang, J.; Lawrence, B.D.; Boyd, J.; Pilkey, A. Effect of microstructure on retained austenite stability and work hardening of TRIP steels. *Mater. Sci. Eng. A* **2011**, *528*, 4516–4521. [[CrossRef](#)]
30. De Moor, E.; Matlock, D.K.; Speer, J.G.; Merwin, M.J. Austenite stabilization through manganese enrichment. *Scr. Mater.* **2011**, *64*, 185–188. [[CrossRef](#)]
31. Lee, S.-J.; Lee, S.; De Cooman, B.C. Mn Partitioning during the Inter-critical Annealing of Ultrafine-Grained 6% Mn Transformation-Induced Plasticity Steel. *Scr. Mater.* **2011**, *64*, 649–652. [[CrossRef](#)]
32. Krauss, G. *Steels Processing, Structure, and Performance*; ASM International: Materials Park, OH, USA, 2005.
33. Hull, D.; Bacon, D. Introduction to Dislocations. *Mater. Today* **2011**, *14*, 502. [[CrossRef](#)]

34. De Cooman, B.C.; Gibbs, P.; Lee, S.; Matlock, D.K. Transmission Electron Microscopy Analysis of Yielding in Ultrafine-Grained Medium Mn Transformation-Induced Plasticity Steel. *Met. Mater. Trans. A* **2013**, *44*, 2563–2572. [[CrossRef](#)]
35. Field, D.M.; Van Aken, D.C. Dynamic Strain Aging Phenomena and Tensile Response of Medium-Mn TRIP Steel. *Met. Mater. Trans. A* **2018**, *49*, 1152–1166. [[CrossRef](#)]
36. Wang, X.; Wang, L.; Huang, M. Kinematic and thermal characteristics of Lüders and Portevin-Le Châtelier bands in a medium Mn transformation-induced plasticity steel. *Acta Mater.* **2017**, *124*, 17–29. [[CrossRef](#)]
37. Dastur, Y.N.; Leslie, W.C. Mechanism of work hardening in Hadfield manganese steel. *Met. Mater. Trans. A* **1981**, *12*, 749–759. [[CrossRef](#)]
38. Lee, S.-J.; Kim, J.; Kane, S.N.; De Cooman, B.C. On the origin of dynamic strain aging in twinning-induced plasticity steels. *Acta Mater.* **2011**, *59*, 6809–6819. [[CrossRef](#)]
39. Cai, Z.H.; Ding, H.; Misra, R.D.K.; Ying, Z.Y. Austenite Stability and Deformation Behavior in a Cold-Rolled Transformation-Induced Plasticity Steel with Medium Manganese Content. *Acta Mater.* **2015**, *84*, 229–236. [[CrossRef](#)]
40. Sun, B.; Vanderesse, N.; Fazeli, F.; Scott, C.; Chen, J.; Bocher, P.; Jahazi, M.; Yue, S. Discontinuous strain-induced martensite transformation related to the Portevin-Le Chatelier effect in a medium manganese steel. *Scr. Mater.* **2017**, *133*, 9–13. [[CrossRef](#)]
41. Callahan, M.; Hubert, O.; Hild, F.; Perlade, A.; Schmitt, J.-H. Coincidence of strain-induced TRIP and propagative PLC bands in Medium Mn steels. *Mater. Sci. Eng. A* **2017**, *704*, 391–400. [[CrossRef](#)]
42. De Moor, E.; Speer, J.G.; Matlock, D.K.; Kwak, J.-H.; Lee, S.-B. Effect of Carbon and Manganese on the Quenching and Partitioning Response of CMnSi Steels. *ISIJ Int.* **2011**, *51*, 137–144. [[CrossRef](#)]
43. Zhang, Y.; Wang, L.; Findley, K.O.; Speer, J.G. Influence of Temperature and Grain Size on Austenite Stability in Medium Manganese Steels. *Met. Mater. Trans. A* **2017**, *48*, 2140–2149. [[CrossRef](#)]
44. Jatczak, C.F.; Larson, J.A.; Shin, S.W. *Retained Austenite and Its Measurements by X-Ray Diffraction, SP-453*; Society of Automotive Engineers: Warrendale, PA, USA, 1980.
45. Addressio, L. The Effect of Strain Rate and Tempering on the Mechanical Properties of Low Carbon Martensite. Master's Thesis, Colorado School of Mines, Golden, CA, USA, 2007.
46. Krauss, G. Heat Treated Martensitic Steels: Microstructural Systems for Advanced Manufacture. *ISIJ Int.* **1995**, *35*, 349–359. [[CrossRef](#)]
47. Swarr, T.; Krauss, G. The effect of structure on the deformation of as-quenched and tempered martensite in an Fe-0.2 pct C alloy. *Met. Mater. Trans. A* **1976**, *7*, 41–48. [[CrossRef](#)]
48. Findley, K.; Hidalgo, J.; Huizenga, R.; Santofimia, M. Controlling the work hardening of martensite to increase the strength/ductility balance in quenched and partitioned steels. *Mater. Des.* **2017**, *117*, 248–256. [[CrossRef](#)]
49. Miller, R.L. Ultrafine-grained microstructures and mechanical properties of alloy steels. *Met. Mater. Trans. A* **1972**, *3*, 905–912. [[CrossRef](#)]
50. Tsuchida, N.; Masuda, H.; Harada, Y.; Fukaura, K.; Tomota, Y.; Nagai, K. Effect of ferrite grain size on tensile deformation behavior of a ferrite-cementite low carbon steel. *Mater. Sci. Eng. A* **2008**, *488*, 446–452. [[CrossRef](#)]
51. Kitamura, H.; Bai, Y.; Tian, Y.; Shibata, A.; Tsuji, N. Deformation Mechanism of Ultrafine-Grained High-Mn Austenitic TWIP Steel. In Proceedings of the International Symposium on New Developments in Advanced High-Strength Sheet Steels, Keystone, CO, USA, 30 May–2 June 2017; AIST: Warrendale, PA, USA, 2017; pp. 315–320.
52. Zavattieri, P.; Savic, V.; Hector, L.G., Jr.; Fekete, J.; Tong, W.; Xuan, Y. Spatio-temporal characteristics of the Portevin-Le Châtelier effect in austenitic steel with twinning induced plasticity. *Int. J. Plast.* **2009**, *25*, 2298–2330. [[CrossRef](#)]
53. Renard, K.; Ryelandt, S.; Jacques, P. Characterisation of the Portevin-Le Châtelier effect affecting an austenitic TWIP steel based on digital image correlation. *Mater. Sci. Eng. A* **2010**, *527*, 2969–2977. [[CrossRef](#)]
54. Shi, J.; Sun, X.; Wang, M.; Hui, W.; Dong, H.; Cao, W. Enhanced work-hardening behavior and mechanical properties in ultrafine-grained steels with large-fractioned metastable austenite. *Scr. Mater.* **2010**, *63*, 815–818. [[CrossRef](#)]
55. Shaw, J.A.; Kyriakides, S. Thermomechanical Aspects of NiTi. *J. Mech. Phys. Solids* **1995**, *43*, 1243–1281. [[CrossRef](#)]
56. Shaw, J.; Kyriakides, S. On the nucleation and propagation of phase transformation fronts in a NiTi alloy. *Acta Mater.* **1997**, *45*, 683–700. [[CrossRef](#)]
57. Ryu, J.H.; Kim, J.I.; Kim, H.S.; Oh, C.-S.; Bhadeshia, H.; Suh, D.-W. Austenite stability and heterogeneous deformation in fine-grained transformation-induced plasticity-assisted steel. *Scr. Mater.* **2013**, *68*, 933–936. [[CrossRef](#)]
58. Gibbs, P.J.; De Moor, E.; Merwin, M.J.; Clausen, B.; Speer, J.G.; Matlock, D.K. Austenite Stability Effects on Tensile Behavior of Manganese-Enriched-Austenite Transformation-Induced Plasticity Steel. *Met. Mater. Trans. A* **2011**, *42*, 3691–3702. [[CrossRef](#)]
59. Mukherjee, M.; Bhattacharyya, T.; Singh, S.B. Models for Austenite to Martensite Transformation in TRIP-Aided Steels: A Comparative Study. *Mater. Manuf. Process.* **2010**, *25*, 206–210. [[CrossRef](#)]
60. Samek, L.; De Moor, E.; De Cooman, B.C.; Van Slycken, J.; Verleysen, P.; Degriek, J. Quasi-adiabatic Effects during the High Strain Rate Deformation of Dispersed-phase Ferrous Alloys with Strain-induced Martensitic Transformation. In Proceedings of the International Conference on Advanced High Strength Sheet Steels for Automotive Applications, Winter Park, CA, USA, 6–9 June 2004; AIST: Warrendale, PA, USA, 2004; pp. 361–374.
61. De Moor, E.; Lacroix, S.; Clarke, A.; Penning, J.; Speer, J. Effect of Retained Austenite Stabilized via Quench and Partitioning on the Strain Hardening of Martensitic Steels. *Met. Mater. Trans. A* **2008**, *39*, 2586–2595. [[CrossRef](#)]

62. Bhadeshia, H.K.D.H.; Edmonds, D.V. Bainite in silicon steels: New composition–property approach Part 1. *Met. Sci.* **1983**, *17*, 411–419. [[CrossRef](#)]
63. Min, J.; Hector, L.G., Jr.; Zhang, L.; Lin, J.; Carsley, J.E.; Sun, L. Elevated-Temperature Mechanical Stability and Transformation Behavior of Retained Austenite in a Quenching and Partitioning Steel. *Mater. Sci. Eng. A* **2016**, *673*, 423–429. [[CrossRef](#)]
64. Krauss, G. Martensite in steel: Strength and structure. *Mater. Sci. Eng. A* **1999**, 40–57. [[CrossRef](#)]
65. Wang, L.Y.; Wu, Y.X.; Sun, W.W.; Bréchet, Y.; Brassart, L.; Arlazarov, A.; Hutchinson, C.R. Thermal and Athermal Contributions to the Flow Stress of Martensite. *Materialia* **2020**, *11*, 100719. [[CrossRef](#)]
66. Bolling, G.; Richman, R. The plastic deformation-transformation of paramagnetic f.c.c. Fe-Ni-C alloys. *Acta Met.* **1970**, *18*, 673–681. [[CrossRef](#)]
67. Richman, R.H.; Bolling, G.F. Stress, deformation, and martensitic transformation. *Met. Mater. Trans. A* **1971**, *2*, 2451–2462. [[CrossRef](#)]
68. Bhadeshia, H.K.D.H. TRIP-Assisted Steels? *ISIJ Int.* **2002**, *42*, 1059–1060. [[CrossRef](#)]
69. Van Rooyen, G. Basic factors which influence the Lüders strain during discontinuous yielding. *Mater. Sci. Eng.* **1971**, *7*, 37–48. [[CrossRef](#)]
70. Matlock, D.K.; Speer, J.G. Design Considerations for the Next Generation of Advanced High Strength Sheet Steels. In Proceedings of the 3rd International Conference on Structural Steels, Gyeongju, Korea, 22–24 August 2006; Lee, H.C., Ed.; The Korean Institute of Metals and Materials: Seoul, Korea, 2006; pp. 774–781.
71. Matlock, D.K.; Speer, J.G. Third Generation of AHSS: Microstructure Design Concepts. In *Microstructure and Texture in Steels and Other Materials*; Haldar, A., Suwas, S., Bhattacharjee, D., Eds.; Springer: London, UK, 2009; pp. 185–205.